Forced convection in the wakes of sliding bubbles

2016 J. Phys.: Conf. Ser. 745 032117

(http://iopscience.iop.org/1742-6596/745/3/032117)

Forced convection in the wakes of sliding bubbles

R O'Reilly Meehan[1,2], B Donnelly[2], T Persoons[1], K Nolan[2], D B Murray[1]

[1]Dept. Mechanical & Manufacturing Engineering, Trinity College Dublin, Ireland
[2]Thermal Management Research Group, Efficient Energy Transfer (ηET) Department, Bell Labs Research, Nokia, Blanchardstown Business & Technology Park, Snugborough Rd, Dublin 15, Ireland.

E-mail: ruoreill@tcd.ie

Abstract.

Both vapour and gas bubbles are known to significantly increase heat transfer rates between a heated surface and the surrounding fluid, even with no phase change. However, the complex wake structures means that the surface cooling is not fully understood. The current study uses high speed infra-red thermography to measure the surface temperature and convective heat flux enhancement associated with an air bubble sliding under an inclined surface, with a particular focus on the wake. Enhancement levels of 6 times natural convection levels are observed, along with cooling patterns consistent with a possible hairpin vortex structure interacting with the thermal boundary layer. Local regions of suppressed convective heat transfer highlight the complexity of the bubble wake in two-phase applications.

1. Introduction

Two phase flows are extremely desirable from a cooling perspective, since they offer extremely high heat transfer coefficients, temperature homogenisation and passive or low power consumptions [1]. However, despite extensive recent research, the widespread implementation of two phase technologies has yet to occur. This is in part due to the complex nature of the flows, which leads to significant uncertainty regarding the reliability of new two phase technologies [1]. This complexity arises from the coupling between the motion of the gas and liquid phases. Current research on two phase bubbly flow has focused on the effect of bubbles moving against horizontal, vertical or inclined surfaces [2, 3, 4, 5, 6, 7]. A key flow configuration for applications such as two-phase shell and tube heat exchangers is the motion of a bubble underneath a heated, inclined surface. Enhanced heat transfer in this configuration has been attributed to the interaction between the bubble and the thermal boundary layer at the surface [7]. Even without phase change, high heat transfer coefficients can be obtained using gas bubbles [3, 5]. However, the surface cooling associated with air bubbles is not fully understood [3].

Freely rising air bubbles can take on different shapes and rise paths depending on the properties of the bubble and the surrounding fluid, namely the Reynolds, Eötvös, and Morton numbers. Typically, oscillations in shape and path triggered by an instability in the bubble wake, which is defined as the region of non-zero vorticity downstream of the bubble [8]. Brücker [9] performed 2-D PIV on ellipsoidal rising bubbles in two 2-D planes, deducing that the structures in three dimensions formed a chain of interconnected vortex loops of alternate circulation

and orientation. These are also known as hairpin vortices and have also been identified as a mechanism in near-wall turbulence [10] and in the flow field surrounding bluff bodies [11], [12].

Bubbles sliding under an inclined surface differ from rising bubbles in that they only experience the component of the buoyancy force parallel to the surface. This is true until the surface inclination angle is increased above a critical angle, at which point they begin to bounce. It is the sliding regime without bouncing that is under consideration here. Maxworthy [13] studied a bubble rising under a flat inclined plate, finding that the terminal sliding velocity did not scale linearly with Reynolds number or surface inclination angle. A later investigation by Perron et al. [14] showed that this terminal velocity instead had distinct regimes corresponding to different bubble shapes. Cornwell [7] identified the main contributions due to heat transfer from a vapour bubble as bubble nucleation, liquid disturbance and micro-layer evaporation. Houston and Cornwell [5] showed that the liquid disturbance induced by a sliding gas bubble with no phase change could account for significant heat transfer at low wall superheats. Qiu & Dhir [15] studied the heat transfer associated with a single vapour bubble as it grew and slid under a downward facing heated surface. The study found that a vortex located immediately behind the bubble enhanced heat transfer from the wall by introducing cooler liquid from the bulk to the surface. This was supported by the 3-D simulations of Li et al. [16]. Donoghue et al. [17] showed that the impact of an air bubble on a horizontal heated surface generated local heat transfer enhancement of up to 18 times natural convection levels.

The current study builds on the recent work of Donnelly et al. [3] and O'Reilly Meehan et al. [2]. Donnelly et al. [3] performed measurements of motion and time-resolved heat transfer coefficient distribution due to a sliding air bubble between 5-9 mm diameter on an inclined heated surface. Bubbles of this size were found to undergo an undulating motion linked to vortex generation and shedding in the bubble wake. Local heat transfer enhancement several times that of natural convection occurred in small regions downstream of the bubble. O'Reilly Meehan et al. [2] performed time-resolved PIV on the wake of a sliding air bubble of 5-7 mm diameter in three measurement planes, revealing a near wake that travelled in close association with the bubble and a far wake that extended downstream in the form of successive hairpin vortex loops. Fluid was found to separate from the near wake at the local extrema of the undulating bubble path, resulting an a large affected region of fluid that overshot the bubble path. The current study seeks to extend this understanding by measuring the convective heat flux of an air bubble sliding under a heated inclined surface, performing an in-depth analysis of the interactions occurring between the bubble, its associated wake and the surface.

2. Experiment

Figure 1 shows the experimental apparatus and a schematic of the flow under investigation. The experimental apparatus in figure 1 (a) consists of a tilting water tank, a heated thin foil and support structure, a bubble injector, and the infrared camera. The water tank is an open top glass cube of dimension 400 $\times$ 400 $\times$ 300 mm^3, filled with distilled water. The heated surface consists of a 25 μm thick, 130 $\times$ 250 mm^2 AISI 316 stainless steel foil, manufactured by Goodfellow. The foil is bonded to a pair of copper busbars using thermally conductive epoxy to ensure good electrical contact and uniform heat generation. A Lambda GENESYS GEN6-200 DC power supply provides 64 amps of constant current to the foil. One of the copper bars is adjustable to tension the foil. On the reverse side of the foil is a window made from sapphire glass, which sits on a ledge 3 mm behind the foil, trapping a small quantity of air. This acts as an infrared transparent insulator, ensuring the majority of the heat generated by the foil is transferred into the water. When heated, the surface provides an approximately constant flux boundary condition, with the difference between surface and bulk temperatures being $T_e = 10K$.

Bubbles are introduced to the surface by an injector system comprising of an acetal copolymer box, gastight syringe (model Hamilton 1000 series GASTIGHT, 5 ml), silicone rubber tubing,

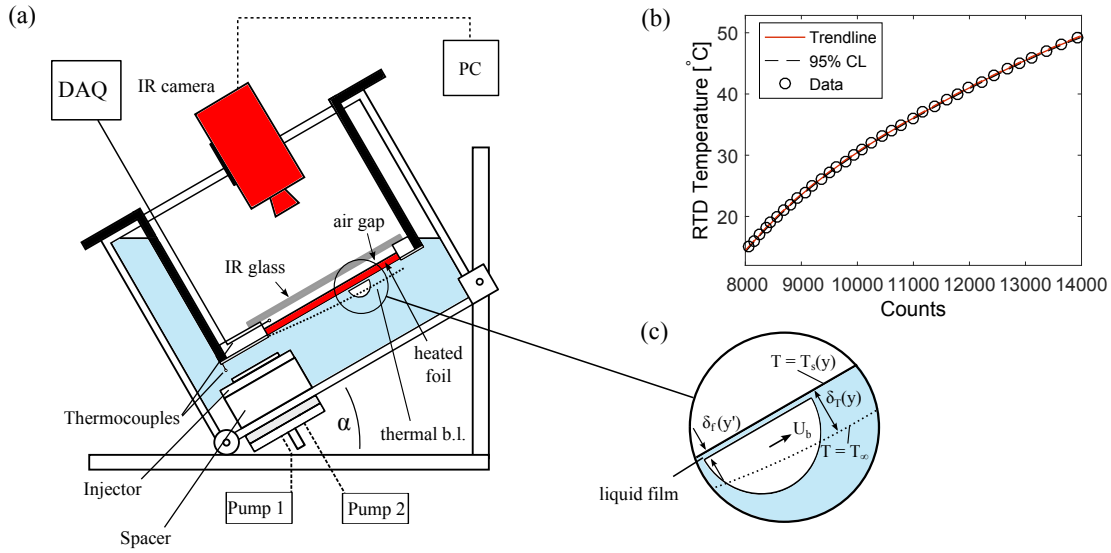

Figure 1. (a) Experimental set-up, (b) in-situ calibration curve and (c) zooming in on the bubble.

a syringe needle, a syringe pump (NE-1000 from New Era Pump Systems, Inc.) and a rotating plate. Inside the box, a series of small bubbles are introduced via the syringe pump and the 5 mm diameter tubing into a cylindrical bubble chamber, coalescing to form a bubble of known size. By rotating a circular plate above this chamber, the bubble is released from the chamber, impacts the surface and slides up into the measurement region. Upon reaching the measurement region, the bubbles are at terminal velocity and are no longer bouncing.

A FLIR SC6000 infrared camera is used to measure the transient changes in surface temperature on the rear of the foil. The camera, which is mounted directly onto the tank, records a 320×256 pixel window of a focal plane array (FPA) sensor at 400 *fps*. The foil is coated in a 25 μm layer of black paint on the air side in order to provide a known, high emissivity. The calibration of the thermal camera is performed in-situ in order to take the effects of paint emissivity and the sapphire window into account. To ensure accurate temperature control during calibration, an open flow loop is formed between the tilting test tank, an external reservoir and a chiller (Grant RC 1400G), which is used to increase the temperature in increments of $1°C$ from $15°C$ to $50°C$. A certified RTD master probe is used as a temperature reference. This calibration curve is shown in figure 1 (b). Finally, a description of this problem is shown in figure 1 (c) by zooming in on the bubble. A liquid film exists between the bubble and surface, which heavily influences the bubble's shape and dynamics. As the bubble slides under the surface, the thermal boundary layer on the underside of the surface is disrupted, changing the heat transfer mechanism to forced convection.

3. Data reduction & uncertainty analysis

To convert from surface temperature into convective heat flux, an energy balance is performed on the raw temperature data from the IR camera in MATLAB. A Biot number analysis on the foil and paint layers shows that a lumped capacitance analysis is appropriate in the current study. An energy balance is subsequently performed on a volume of foil of dimensions (i.e. $dx \times dx \times \delta$), where δ is the foil and paint thickness and dx is width of a pixel on the FPA. This is performed on every pixel of the surface temperature plot, yielding:

$$q''_{conv} = q''_{gen} - q''_{cond} - q''_{rad} - (\rho_f c_{p,f} \delta_f + \rho_p c_{p,p} \delta_p) \frac{\partial T}{\partial t} + (k_f \delta_f + k_p \delta_p) \left(\frac{\partial^2 T}{\partial x^2} + \frac{\partial^2 T}{\partial y^2} \right) \quad (1)$$

where k_f, k_p, ρ_f, ρ_p, $c_{p,f}$ and $c_{p,p}$ are the stainless steel and paint thermal conductivity, density and specific heat capacity, respectively. This equation accounts for the generated heat flux (q''_{gen}), the one-dimensional conduction through the 3 mm air gap to the IR glass (q''_{cond}) and the radiation from the surface on the air side (q''_{rad}). Lateral conduction and heat storage within the foil and paint layer are also accounted for in equation 1. These terms are solved by applying a second order central-difference approximation to the spatial derivatives and a central-difference approximation to the temporal derivatives. To prevent excess noise, the spatial derivatives are weighted using a Gaussian filter generated from Pascal's triangle ($n = 5$) before differentiation.

To find the propagation of errors in the convective heat flux measurement, the Taylor series method, as described by Coleman & Steele [18], is applied to each term in the foil energy balance. This method takes into account the uncertainties of the curves fitted to the calibration of the IR camera and the thermocouples, the precision of the current measurements and the foil and paint properties. An additional, covariance term is added to the lateral conduction and the heat storage terms, since these terms involve operations between adjacent pixels on the FPA in space and time, respectively. The degree of correlation is found by applying an autocorrelation analysis on the temporal derivatives in the heat storage term and a cross-correlation analysis on the spatial derivatives in the lateral conduction term. The resultant uncertainties are shown in table 1. These values are consistent with those of Donnelly et al. [3] and Donoghue et al. [17].

Table 1. Absolute and relative uncertainty for the measured thermal data.

Measurement	Symbol	Absolute Uncertainty	Relative Uncertainty [%]
Surface temperature	T_s	0.14° C	–
Water temperature	T_∞	0.12° C	–
Air temperature	T_a	0.15° C	–
Convective heat flux: near wake	q''_{conv}	800 - 1400 W/m^2	9 – 11
Convective heat flux: far wake	q''_{conv}	340 - 800 W/m^2	11 – 20

4. Results

In this section, the surface temperature and convective heat flux are presented for bubbles of diameter $d_e = 5.7$ and 7.2 mm sliding under a heated surface inclined at $\alpha = 30°$ to the horizontal, at a mean wall superheat of $T_e \approx 10K$. The temperature plots are expressed in terms of the non-dimensional surface temperature ΔT^*. This is given by $\Delta T^* = \frac{T_s - T_\infty}{T_0 - T_\infty}$, where T_s is the current surface temperature, T_0 is the surface temperature with no bubble present and T_∞ is the bulk fluid temperature. The convective heat flux is similarly non-dimensionalised and can be considered as an enhancement ratio of forced to natural convection, $q^* = \frac{q''_{conv}}{q''_{nat}}$. Note that although the bubble position is not tracked, it can be found based on the motion observed by the authors in previous work [2, 3]. Reference to the bubble and fluid velocities are also based on the findings of these earlier studies.

Figure 2 shows the dimensionless surface temperature and enhancement ratio at two instances in time 0.2 s apart for $d_e = 5.8$ mm and 7.2 mm. The bubble forms a "snake"-like cooled region

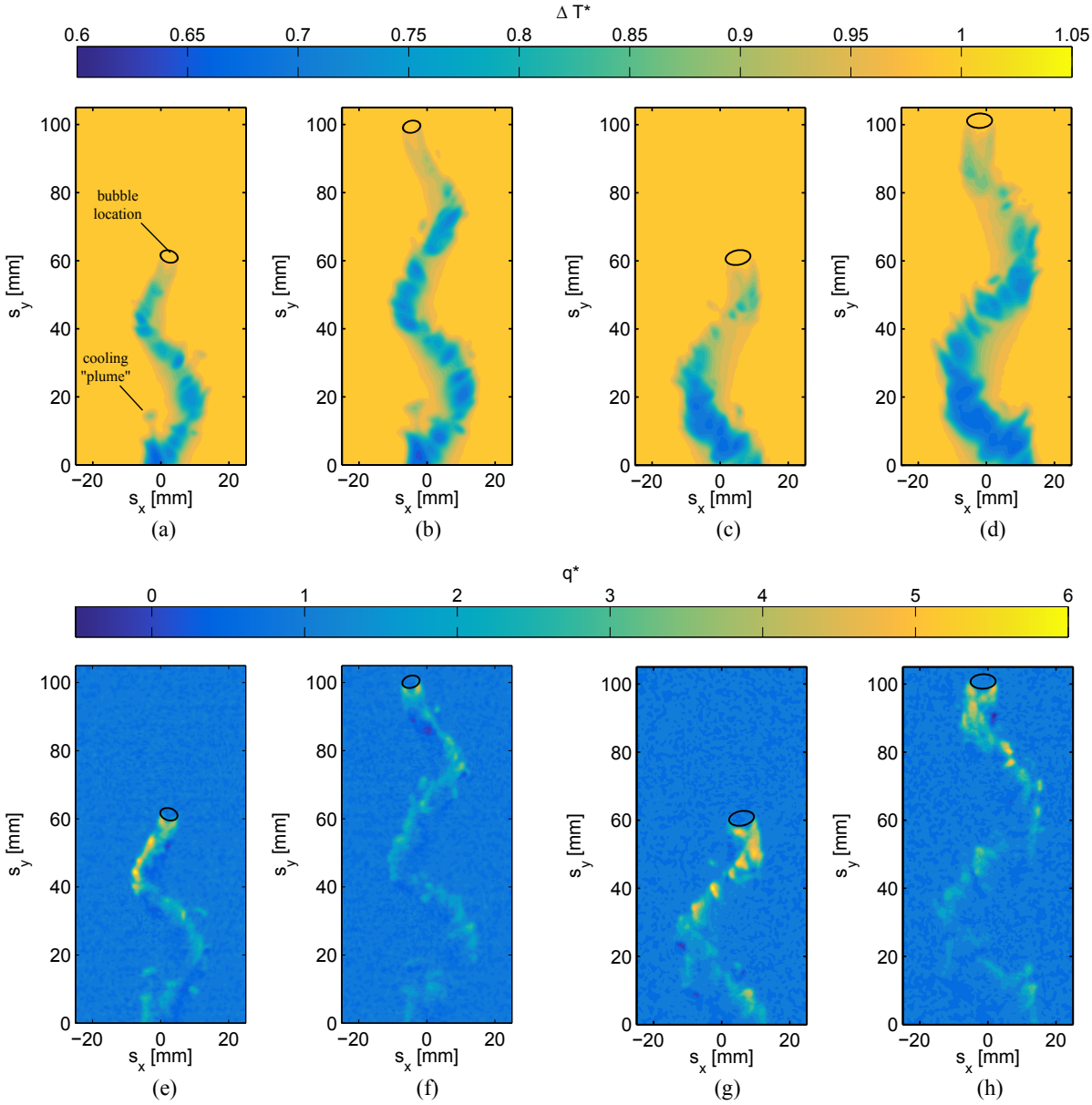

Figure 2. Dimensionless temperature ΔT^* (a-d) and convective flux enhancement $q*$ (e-h) at instances in time 0.2 s apart for $\alpha = 30°$ and $d_e = 5.8$ mm (a,b,e,f) and $d_e = 7.2$ mm (c,d,g,h). The mean superheat is initially $T_e = 10K$.

that is advected along the length and spanwise directions, overshooting the bubble path and spreading over the foil. In the temperature plot in figure 2 (a), the bubble is initially at the position $s_y \approx 60$ mm. In the wake of the bubble is an extended region of reduced surface temperature, which is approximately the width of the bubble base immediately to the rear of the bubble and widens to approximately 1.5 bubble diameters at the base of the interrogation window. At this point, the lowest surface temperature is observed as the thermal boundary layer is at its thinnest. The surface temperature is comparatively high at the bubble location, implying that the surface cooling is caused by the near wake of the bubble introducing fresh fluid from the bulk to the surface. In the far wake downstream, interactions between this fluid

and the thermal boundary layer cause secondary cooling structures, such as the "plume" shaped region of surface cooling highlighted on figure 2 (a).

The convective heat flux enhancement shown in figure 2 (c) reveals regions of local convective heat flux enhancement in the near wake that start directly to the rear of the bubble and can extend over 4-5 bubble diameters downstream. Typically, large convective heat transfer corresponds to regions with a high fluid velocity in the wake, although heat flux enhancement is also observed in the slow-moving far wake. At the bubble, the convective heat transfer forms a triangular-shaped region that starts at the bubble major axes. Downstream of the bubble, local heat flux enhancements of up to 6 times natural convection levels are visible on the outside of the wake structure. The regions of maximum convective cooling take the form of small, approximately elliptical locations within the wake structure. Further downstream in the far wake, the heat flux has reduced to ≈ 2.5 times that of natural convection levels at the base of the interrogation window. Interestingly, to the rear of the bubble on the inside of its path is a region of suppressed heat flux, where the local temperature is recovering.

At 0.2 s later (figure 2 (b) and (f)), the surface temperature in the far wake has reduced further, although the convective heat transfer has now dropped to under twice that of natural convection levels. Note that the convective flux enhancement behind the bubble appears lower than that at the first instant in tine. This is due to the increased thickness of the thermal boundary layer at the top of the foil, which reduces the relative enhancement effect. As the cooled region temporally evolves, it is advected up the foil at a significant rate, which is due to the fluid motion within the thermal boundary later at the surface. In the far wake, the smaller regions of low surface temperature eventually begin to join together into larger elliptical regions, with cooling effects lasting up to 20 seconds after the bubble passage. The specific heat capacity of the water and low wall superheat means that it takes some time for the surface to recover from this thermal depression. Thus, the mode of convective heat flux in the low-velocity far wake reverts to natural convection but remains larger than the base levels due to the bubble having introduced cooler fluid to the surface.

The effect of increasing the bubble diameter to 7.23 mm on ΔT^* (figure 2 (b) and (c)) and q^* (figure 2 (g) and (h)) is to provide greater fluid advection and a larger affected area of enhancement, although the level of surface cooling and heat flux enhancement is largely similar to the 5.8 mm test. The greater bulk motion of the fluid leads to higher values of convective flux in the far wake, while secondary flow features are again visible at the extrema of the bubble path. Note again that the maximum convective heat transfer occurs in small, elliptical packets that are visible along the outside of the bubble path up to 5 diameters downstream of the bubble. Thus, at a nominal wall superheat of $10°C$, the influence of increasing the bubble volume on surface temperature is to provide surface cooling over a larger area, rather than decreasing the local temperature further.

Figure 2 revealed complex, transient regions of both convective heat transfer enhancement and suppression in the near wake of the bubble. Figure 3 focuses on these regions in greater detail by plotting the instantaneous convective heat flux in the near wake of the 5.8 mm bubble at 10 ms intervals. Some trends in the convective heat flux are apparent. In general, with increasing distance along the surface, the local heat transfer decreases due to the increasing thermal boundary layer thickness. As the bubble traverses the surface, distinct variations occur in the local convective heat flux, which are linked to the path-wise location of the bubble. Directly after an extremum in bubble path, high convective heat flux is observed just downstream of the bubble in the near wake. As the bubble returns from this extremum to its mean position, there is comparatively little enhancement in the near wake. This behaviour is consistent with a wake structure that sheds from the bubble at the extrema in path, which was shown by Brücker [9] to occur for freely rising bubbles. As was discussed in relation to figure 2, convective heat transfer enhancement starts at the bubble major axes and extends back in a v-shaped

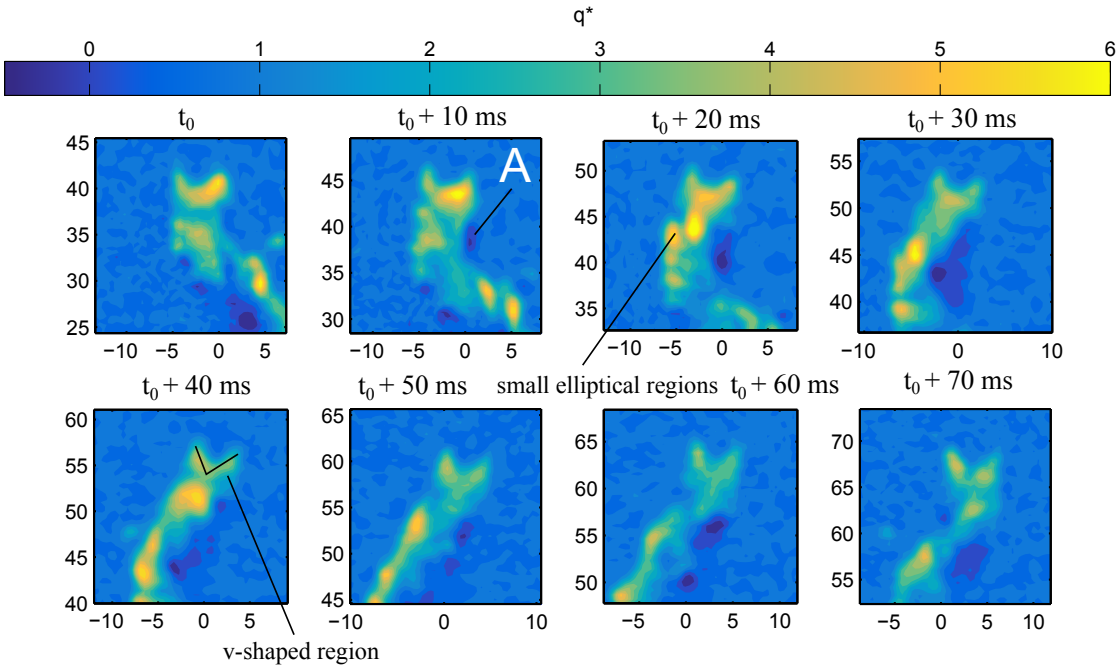

Figure 3. Convective flux enhancement, q^*, in the near wake for $\alpha = 30°$, $d_e = 5.8\ mm$ provided at instances in time 10 ms apart. The axes limits are in mm.

region, resulting in comparatively low convective heat flux at the base of the bubble minor axis. Downstream of the bubble, the convective heat transfer enhancement takes the form of small elliptical regions within the near wake, which could conceivably be the various components of a hairpin vortex impacting the surface, as observed by Acalar and Smith for a hemispherical protrusion on a flat plate [11]. Since the fluid travelling in the near wake is spreading outwards, it follows that the majority of this enhancement occurs on the outside of the wake.

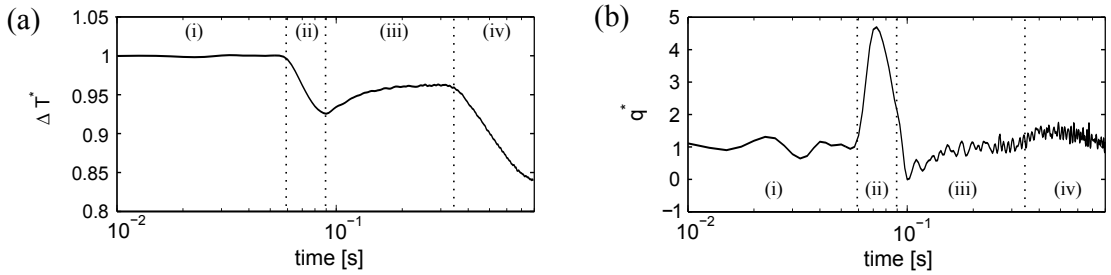

Figure 4. Plot of (a) the dimensionless temperature ΔT^* and (b) convective flux enhancement $q*$ for $d_e = 5.8\ mm$, $\alpha = 30°$ as a function of time for the key location A on figure 3.

On the inside of the near wake, small regions of suppressed, even negative heat flux are visible. Consider the region of suppressed convective flux denoted as A in the second image in figure 3. The evolution of surface temperature and convective heat flux at this location are provided in figure 4. Before the bubble passage (figure 4, period (i)), ΔT^* and q^* are approximately unity. At time (ii) on figure 4, the bubble passes through the point A as it approaches its local minimum in path, resulting in high convective flux levels and a decrease in surface temperature at A. As the bubble reaches its local minimum, the bubble changes direction and its near wake

separates, continuing to move in the negative spanwise direction. Thus, although the bubble passes through A, its near wake does not. Since there is no cool fluid at the location A, its surface temperature recovers, resulting in suppressed (or in some cases, negative) convective heat flux. This behaviour is visible on figure 4 (iii). Finally, a further reduction in surface temperature is observed where the wake downstream is advected into the region A. This repeats as the bubble traverses the surface; namely the development of regions of low heat flux at regions where the bubble passed through but its wake does not. Note that this suppressed convective heat transfer only occurs following a period of initial convective heat transfer enhancement. Thus, the overall effect of the sliding bubble is to increase convective heat transfer and decrease the mean surface temperature.

5. Conclusion

This work has presented a study of the convective heat transfer enhancement offered by a sliding bubble by means of high-speed infra-red thermography at a nominal wall superheat of $T_e = 10°C$. Heat transfer enhancement occurs via bluff body advection and due to the near wake introducing fluid from the bulk to the surface. In the near wake, enhancement levels were observed of up to 6 times that of natural convection, with a cooling pattern consistent with that of a hairpin vortex impacting the surface. Local heat flux measurements also reveal small regions of suppressed heat transfer at locations through which the bubble, but not its wake, passes. Thus, although sliding air bubbles increase convective heat transfer rates (in this study, local enhancements from $2kW/mK$ to 12 kW/mK were observed for both diameters), the interaction between the bubble wake and the thermal boundary layer is complex and warrants further investigation.

Acknowledgements

This research is supported by the Irish Research Council under its Enterprise Partnership scheme, grant number EPSPG/2012/323, in association with Bell Labs Ireland. Bell Labs Ireland would like to thank the Industrial Development Agency (IDA) Ireland for their financial support.

References

[1] Robinson A J 2009 *Components and Packaging Technologies, IEEE Transactions on* **32** 347–357
[2] O'Reilly Meehan R, Donnelly B, Persoons T and Murray D B 2016 *Int. J. of Multiphase Flow* **84** 145–154
[3] Donnelly B, O'Reilly Meehan R, Nolan K and Murray D B 2015 *Int. J. of Heat and Mass Transfer* **91** 532–542
[4] Donoghue D, Donnelly B and Murray D B 2012 *J. of Enhanced Heat Transfer* **19**
[5] Houston S and Cornwell K 1996 *Int. J. of Heat and Mass Transfer* **39** 211–214
[6] Yan Y, Kenning D, Grant I and Cornwell K 1995 *Inst. of Mech. Engineers Conf. Pub.* vol 2 pp 295–295
[7] Cornwell K 1990 *Int. J. of Heat and Mass Transfer* **33** 2579–2584
[8] Fan L and Tsuchiya K 1990 *Bubble wake dynamics in liquids and liquid-solid suspensions* (Butterworth-Heinemann Stoneham)
[9] Brücker C 1999 *Phys. of Fluids* **11** 1781
[10] Adrian R and Liu Z 2002 *J. of Visualization* **5** 9–19
[11] Acarlar M and Smith C 1987 *J. of Fluid Mech.* **175** 1–83
[12] Stewart B, Thompson M, Leweke T and Hourigan K 2010 *J. of Fluid Mech.* **643** 137–162
[13] Maxworthy T 1991 *J. of Fluid Mech.* **229** 659–674
[14] Perron A, Kiss L and Poncsák S 2006 *Int. J. of Multiphase Flow* **32** 606–622
[15] Qiu D and Dhir V 2002 *Exp. Thermal and Fluid Science* **26** 605–616
[16] Li D, Manickam S and Dhir V 2005 *ASME Summer Heat Transfer Conf., San Francisco*
[17] Donoghue D, Albadawi A, Delauré Y, Robinson A and Murray D B 2014 *Int. J. of Heat and Mass Transfer* **71** 439 – 450
[18] Coleman H W and Steele W G 2009 *Experimentation, validation, and uncertainty analysis for engineers* (John Wiley & Sons)